

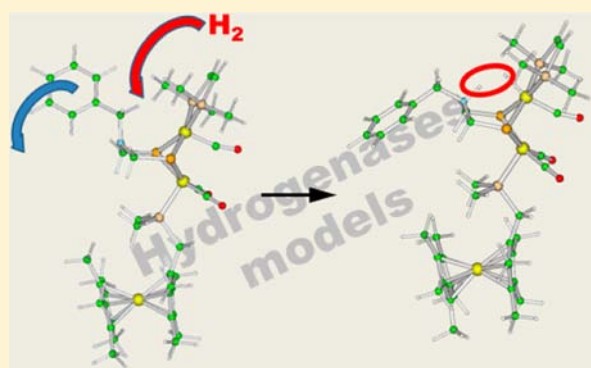
H₂ Binding and Splitting on a New-Generation [FeFe]-Hydrogenase Model Featuring a Redox-Active Decamethylferrocenyl Phosphine Ligand: A Theoretical Investigation

Claudio Greco*

Institut für Chemie, Humboldt-Universität zu Berlin, Brook-Taylor strasse 2, 12489 Berlin (Germany) and Department of Environmental and Earth Sciences, Università degli Studi di Milano-Bicocca, Piazza della Scienza 1, 20126, Milano, Italy

S Supporting Information

ABSTRACT: [FeFe]-hydrogenases are dihydrogen-evolving metalloenzymes that are able to combine substrate binding and redox functionalities, a feature that has important bearing on their efficiency. New-generation bioinspired systems such as Fe₂[(SCH₂)₂NBn](CO)₃(Cp*Fe(C₅Me₄CH₂PEt₂))(dppv) were shown to mimic H₂ oxidation and splitting processes performed by the [FeFe]-hydrogenase/ferredoxin system, and key mechanistic aspects of such reaction are theoretically investigated in the present contribution. We found that H₂ binding and heterolytic cleavage take place concomitantly on DFT models of the synthetic catalyst, due to a substrate-dependent intramolecular redox process that promotes dihydrogen activation. Therefore, formation of an iron-dihydrogen complex as a reaction intermediate is excluded in the biomimetic system, at variance with the case of the enzyme. H₂ uptake at the synthetic system also requires an energetically disfavored isomerization of the amine group acting as a base during splitting. A possible strategy to stabilize the conformation competent for H₂ binding is proposed, along with an analysis of the reactivity of a triiron complex in which di(thiomethyl)amine—the chelating group naturally occurring in [FeFe]-hydrogenases—substitutes the benzyl-containing dithiolate ligand.



INTRODUCTION

Extensive research efforts are currently devoted to the design and characterization of efficient and green catalytic paths for molecular hydrogen production and splitting.¹ In fact, such reversible reaction might be relevant for development of next-generation, eco-compatible approaches for energy storage and utilization. Notably, several microorganisms have an active dihydrogen metabolism in which specific metalloenzymes generally termed hydrogenases play the main role.² Three hydrogenase classes are known to date, but only two of them—the [FeFe]- and [NiFe]-hydrogenases—exploit the redox activity of their active site to catalyze the reaction $\text{H}_2 \rightleftharpoons 2\text{H}^+ + 2\text{e}^-$; the third class—the [Fe]-hydrogenases—instead requires the presence of an exogenous hydride acceptor to activate H₂.³

[FeFe]-hydrogenases are the most efficient catalysts for biological evolution of dihydrogen.⁴ As suggested by their name, the active site of these enzymes is characterized by the presence of a diiron assembly (usually termed [2Fe]_H),^{5–7} which is covalently linked to a ferredoxin-like Fe₄S₄ cubane (the so-called [4Fe-4S]_H subsite, see Figure 1). These two subclusters constitute a Fe₆S₆ site which is conserved in all the [FeFe]-hydrogenases characterized to date and is referred to as the H-cluster. The [2Fe]_H site is peculiar from a biochemical point of view: it includes a dithiolate bridge

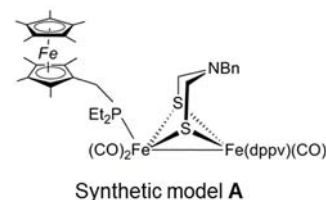
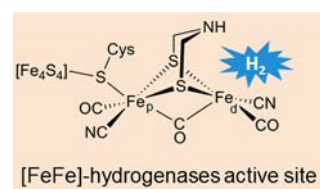


Figure 1. Schematic structures of [FeFe]-hydrogenases active site and of the bioinspired model A (Bn = CH₂Ph, dppv = *cis*-C₂H₂(PPh₂)₂). Site for H₂ binding and activation in the enzyme active site is highlighted.

between metal ions as well as the biologically unusual carbonyl and cyanide ligands. Recent theoretical and experimental

Received: September 28, 2012

Published: February 1, 2013

results⁸ produced convincing evidence of the fact that the dithiolate ligand is actually di(thiomethyl)amine (dtma). The amine group of the latter is thought to exert an important role as an acid–base group during catalysis. In fact, it was shown to be able to mediate facile proton transfers toward and from one of the iron atoms of the $[2\text{Fe}]_{\text{H}}$ subsite (see the upper half of Figure 1). Such iron center of the $[2\text{Fe}]_{\text{H}}$ subsite will be referred to as “distal” (Fe_{d} , see Figure 1) in order to distinguish it from the proximal iron ion (Fe_{p}) that is relatively closer to the $[4\text{Fe}-4\text{S}]_{\text{H}}$ subsite. The enzyme form ready to accept protons and to start the enzymatic process in the reductive direction is H_{red} , which attains the $\text{Fe}(\text{I})\text{Fe}(\text{I})$ state at the diiron assembly. The form which undergoes H_2 binding is termed H_{ox} instead, which features a mixed-valence, $\text{Fe}(\text{II})\text{Fe}(\text{I})$ $[2\text{Fe}]_{\text{H}}$ subsite.⁹

Notably, recent theoretical results indicate that $[\text{FeFe}]$ -hydrogenases are able to couple H_2 binding to the bimetallic active site with one-electron oxidation of the latter;¹⁰ this in turn increases dihydrogen acidity, thus favoring its splitting. Concerted transfers of protons and electrons are also expected to play a crucial role in the H^+ reduction mechanism, leading to H_2 evolution.^{9,11} All electron-transfer events toward and from the $[2\text{Fe}]_{\text{H}}$ assembly are mediated by the $[4\text{Fe}-4\text{S}]_{\text{H}}$ subsite and by ancillary protein-embedded iron–sulfur clusters that usually flank the H-cluster (Figure 2).^{9,12}

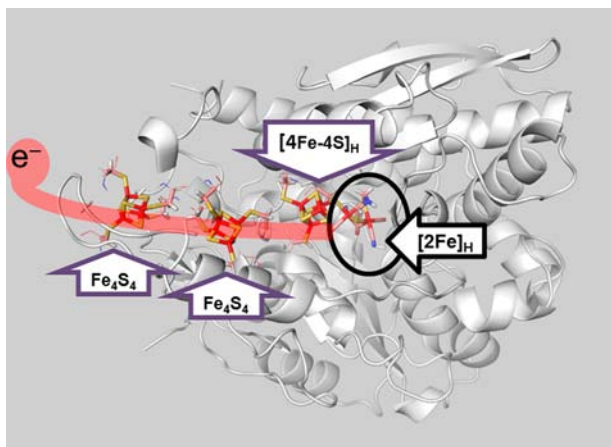
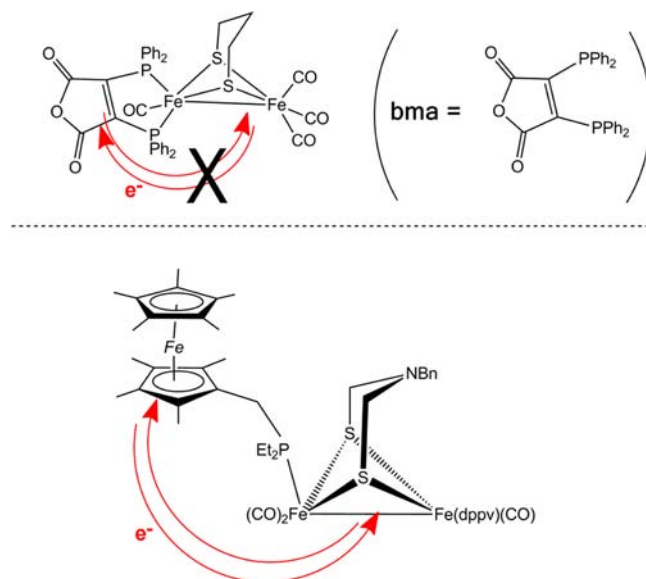


Figure 2. Ribbon representation of $[\text{FeFe}]$ -hydrogenase crystal structure from *D. desulfuricans*.⁶ Path for electron transfer is highlighted with a transparent red strip. Each metal–sulfur assembly included in the protein matrix is highlighted by an arrow.

Given the crucial redox function that these Fe_4S_4 cubanes exert, reproduction of their effects in biomimetic complexes represents an important and challenging target for bioinspired synthesis.^{13–16} One of the first attempts to install a redox-active group on a biomimetic diiron carbonyl cluster has been reported by Gloaguen and co-workers,¹³ who synthesized and characterized a species including the 2,3-bis-(diphenylphosphino)maleic anhydride (bma, see Scheme 1).¹⁷ With respect to typical phosphine ligands previously used in biomimetic complexes,¹⁸ bma novelty resides in the availability of a low-lying π^* orbital delocalized on the maleic anhydride ring, ready to accept reducing equivalent(s) at relatively mild potentials. However, it was shown that the bma ligand is unable to establish relevant electronic communication with the metal centers in such tetracarbonyl dithiolate-bridged complex, and no proton-induced electron transfers from the

Scheme 1. (Top) Schematic Structure of the Tetracarbonyl Complex Including 2,3-Bis(diphenylphosphino)maleic Anhydride (bma, see inset); (Bottom) Drawing of the Biomimetic Compound Recently Obtained by Camara and Rauchfuss^{14a}



^aRed arrows illustrate the redox interplay between noninnocent ligand and the Fe_2 core, which is absent in the bma-containing model, at variance with the case of the triiron species.

bma ligand to the diiron core turned out to be possible in this case (Scheme 1, upper half).^{13,19}

Density functional theory calculations can give important hints for the design of synthetic models with enhanced redox properties, as shown recently.^{16,19,20} In particular, theory allowed us to propose that installing metallocenes on diiron complexes through a phosphine bridge can favor intramolecular electron transfers functional for reversible oxidation of H_2 .¹⁹ Notably, Camara and Rauchfuss recently incorporated a decamethylferrocene derivative on a diiron cluster mimicking the $[\text{FeFe}]$ -hydrogenases active site.¹⁴ As a result, they obtained the first example of a biomimetic cluster combining redox and substrate binding functionalities, leading to a remarkable reproduction of the enzyme function. This complex in its neutral form (**A**, Figure 1) attains the $\text{Fe}(\text{II})$ redox state at the level of the metallocene sandwich, while the diiron subunit is in the $\text{Fe}(\text{I})\text{Fe}(\text{I})$ state. Upon monoelectronic oxidation ($\text{A} \rightarrow \text{A}^+ + e^-$), the latter subunit shifts to the mixed-valence $\text{Fe}(\text{II})\text{Fe}(\text{I})$ state, with concomitant terminal to semibridging movement of one of the CO groups in the diiron site. A second oxidation step was shown to correspond to the metallocene/metallocenium couple; the resulting dicationic adduct A^{2+} is able to bind and split exogenous molecular hydrogen rapidly, much more efficiently than any other all-iron biomimetic complex previously tested for this kind of reactivity.^{21,22}

Fifteen years after the first report of $[\text{FeFe}]$ -hydrogenases crystal structure,⁵ synthesis of a biomimetic complex such as **A** represents a major breakthrough toward obtainment of a complete functional model of this hydrogenase class.²³ In such context, density functional theory not only can provide fundamental insights on the mechanistic aspects of the interaction between H_2 and **A** but also allows us to compare details of the reactivity of the latter and of other bioinspired

species. These are the main aims of the present theoretical investigation, which also reports a comparison between the novel outcomes on **A** and previous theoretical results on H_2 binding and splitting at the enzyme active site.

METHODS

All geometry optimizations, relative energy calculations, prediction of charge transfer events, vibrational frequency computations, and their scaling were carried out using approaches previously applied or specifically developed and validated in our laboratories for the study of hydrogenases models.^{19,24–26} In particular, geometry optimizations were based on in-vacuum density functional theory (DFT) calculations carried out using the Turbomole program suite²⁷ at the BP86-RI/TZVP level,²⁸ an approach that provides very good performances in terms of reproduction of structural features of hydrogenases models (see refs 25 and 29 and *vide infra*). As far as the atomic composition of the DFT model is concerned, to reasonably reduce the computational cost we decided to locally modify the ligands in **A** as follows: the bis(diphenylphosphino)ethylene moiety bound to one of the Fe centers in **A** has been replaced with a bis(dimethylphosphino)ethylene ligand. Moreover, the ethyl groups in the trialkylphosphine substituent bound to the metallocene portion of **A** have been replaced with methyl groups. Calculations on selected models, left unmodified with respect to the original atomic composition of **A**, showed that the above-described modifications of ligands lead to negligible variation of the overall theoretical picture (see Supporting Information).

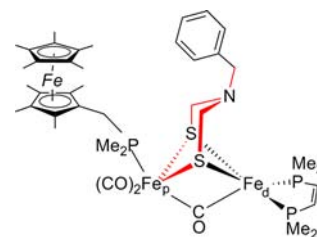
For all models, stationary points of the energy hypersurface have been located by means of energy gradient techniques, and full vibrational analyses have been carried out to further characterize each stationary point; spurious imaginary vibrations around or below 20i cm^{-1} persisted in some models also after targeted reoptimizations employing the dedicated *screw* utility of Turbomole and were therefore ignored as products of numerical inaccuracies.³⁰ The IR parameters here reported for all-iron models were obtained by scaling the computed BP86-RI/TZVP frequencies according to a method specifically developed for [FeFe]-hydrogenases.²⁶ Optimization of transition state structures has been carried out according to a procedure based on a pseudo-Newton–Raphson method, as previously described.³¹ The antiferromagnetic coupling of opposite spins that characterize several of the discussed species has been modeled using the broken symmetry (BS) approach.³² Single-point B3LYP³³ calculations at the BP86-RI/TZVP geometry were carried out to compute Mulliken charges and spin populations (also in this case, the TZVP basis was employed); as shown previously,¹⁹ this approach gives a reliable picture on intramolecular redox events, as the hybrid functional provides superior performance in describing electron delocalization.³⁴ Electron transfers within models were investigated by computing the overall Mulliken charges and spin populations of selected fragments within DFT models. The composition of such sites will be defined by dedicated schematic drawings in the Results and Discussion.

RESULTS AND DISCUSSION

Before illustrating our findings, let us point out the details of the nomenclature used in the following. All DFT models will be termed with bold-face lowercase letters in order to distinguish them from experimental counterparts. For the latter, bold-face uppercase letters will be used. Different isomers of the same species will be tagged with progressive numbers, and the overall charge of ionic models will be explicitly shown. In full analogy with the enzyme active site, the metal centers in the diiron subunit of **A** will be termed “proximal” or “distal” (Fe_p or Fe_d) according to their relative distance with respect to the metallocene fragment. Finally, **A** features a tertiary amine covalently bound to a benzyl substituent; the benzyl group can reside in the *equatorial* position with respect to the $\text{N}-\text{C}_2-\text{S}_2-$

Fe_p ring, as in Scheme 2. The alternative geometry will be referred to as *axial*.

Scheme 2. Initial Structure for the Geometry Optimization of **A**^a



^aRed bonds highlight the equatorial position of the benzyl substituent in this scheme.

Theoretical Results on Structure and Reactivity of the All-Iron Model **A and Derivatives.** The [FeFe]-hydrogenases model **A** was experimentally shown to attain the Fe(II) redox state at the metallocene sandwich, while the diiron fragment was found to enjoy the Fe(I)Fe(I) redox state; in conformity with a previous report,¹⁴ we will refer to this state as Fe(II)Fe(I)Fe(I). Notably, the Fe(I)Fe(I) state is characteristic of the H_{red} enzyme form, which features a carbonyl in the semibridging position between the metal centers of the diiron unit.³⁵ However, the IR spectrum of **A** does not indicate the presence of semibridging carbonyl groups,¹⁴ meaning that all CO ligands occupy terminal positions. In order to investigate the coordination geometry of **A**, we carried out the energy minimization of a DFT model initially featuring a μ -CO group (Scheme 2).

Notably, the μ -CO ligand detaches from Fe_p along relaxation, reaching a 3.34 Å distance from Fe_p upon convergence (model **a** in Figure 3). Overall charge and spin populations of the diiron and metallocene fragments were also computed and reported in Table 1; they are consistent with the Fe(II)Fe(I)Fe(I) state. Model **a** was also considered for vibrational frequencies calculation: the computed CO vibrational frequencies, scaled according to ref 26 as explained in Methods, are 1959, 1906, and 1896 cm^{-1} (Table 2). They compare well with the intense experimental bands at 1958 and 1907 cm^{-1} and with the shoulder observed at 1897 cm^{-1} . Finally, as far as the geometry of the amine in the pendant is concerned, an isomer of **a** with the alternative axial position of the benzyl group was also optimized (structure shown in the Supporting Information), and it turned out to be disfavored by 2.9 kcal mol^{-1} .

Exposing **A** to acids leads to formation of $\text{A}^+-\mu\text{H}$, a bridging-hydride compound formally attaining the Fe(II)Fe(II) state at the diiron site. The corresponding DFT model ($\text{a}^+-\mu\text{H}$, Figure 3) was optimized, and the Mulliken population analysis we performed indicates charge delocalization on the diiron and the mononuclear fragments (Table 1). Computed vibrational frequencies for $\text{a}^+-\mu\text{H}$ are positioned at 1965, 1970, and 2016 cm^{-1} . The corresponding experimental spectrum features only two bands instead (Table 2); the broader and more intense one is at 1973 cm^{-1} , and theory suggests that it originates from superimposition of the two bands at lower wavenumbers in our model.

A can also undergo one-electron oxidation giving rise to A^+ , an adduct featuring a carbonyl ligand in the semibridging position within the diiron portion. The latter attains the Fe(II)Fe(I) redox state, which is also typical of the H_{ox} form

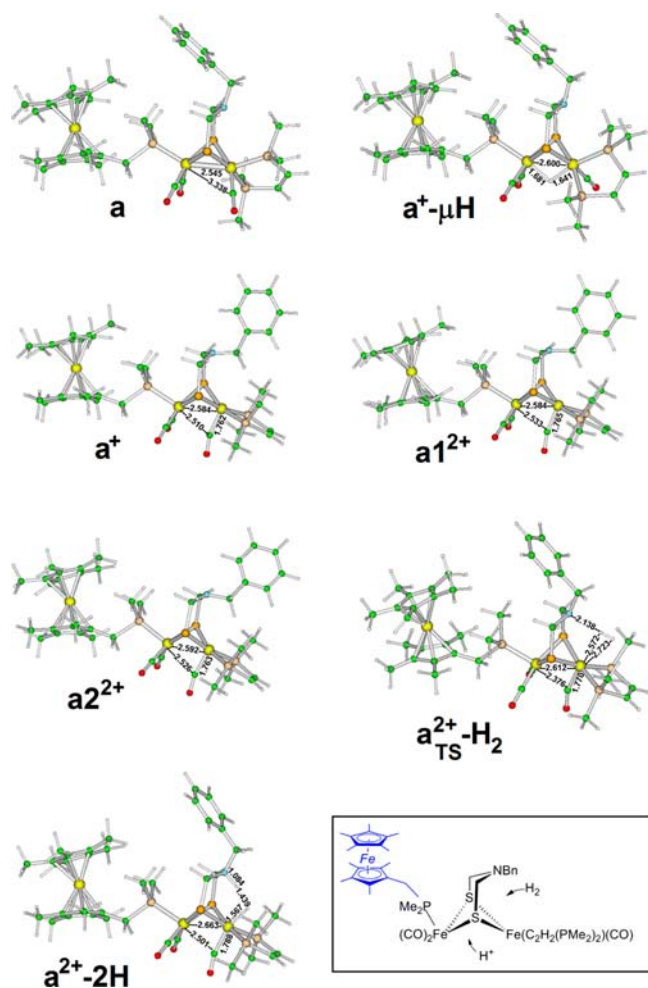


Figure 3. Optimized structures of selected triiron models, with relevant bond distances explicitly marked (all values in Angstroms). Atom colors are as follows: Fe, yellow; S, brownish-yellow; P, wheat; C, green; N, light blue; O, red; H, white. (Inset) Generic schematic representation of the models: composition of the diiron and monoiron portions considered for Mulliken population analyses (see Table 1) is highlighted in black and blue, respectively.

Table 1. Overall Mulliken Spin Populations and Charges (the latter in parentheses, expressed in elementary units e) of the Mononuclear and Dinuclear Portions of the All-Iron Models

compound	dinuclear portion	mononuclear portion
a	0.00 (0.07)	0.00 (−0.07)
$a^+ - \mu\text{H}$	0.00 (0.46)	0.00 (0.54)
a^+	0.97 (0.95)	0.00 (0.04)
$a1^{2+}$	0.96 (1.11)	1.01 (0.89)
$a2^{2+}$	0.96 (1.09)	−1.01 (0.91)
$a^{2+} - 2\text{H}$	0.00 (1.85)	0.00 (0.15)
a_dtma	0.00 (−0.06)	0.00 (0.06)
a_dtma^+	0.96 (0.96)	0.01 (0.04)
$a1_dtma^{2+}$	0.97 (1.09)	1.01 (0.91)
$a2_dtma^{2+}$	0.97 (1.09)	−1.01 (0.91)
$a_dtma^{2+} - \text{H}_2$	0.00 (1.71)	0.00 (0.28)
$a_dtma^{2+} - 2\text{H}$	0.00 (1.80)	0.00 (0.20)

of [FeFe]-hydrogenases.⁹ Not differently from the experimental picture, optimization of the cationic model a^+ gives rise to a geometry featuring a CO group in the semibridging position

Table 2. Theoretical Frequencies for CO Stretching Modes in Selected Triiron Models, and Corresponding Experimental Values (in cm^{-1})^{14 a}

model	experimental frequencies	theoretical frequencies and intensities
a	1958, 1907, 1897	1959 (1540), 1906 (1049), 1896 (814)
$a^+ - \mu\text{H}$	1973, 2018	1965 (254), 1970 (745), 2016 (569)
a^+	2014 ^b , 1963 ^b , 1867 ^b	1998 (810), 1959 (420), 1871 (1082)
$a1^{2+}$	2017 ^b , 1967 ^b , 1852 ^b	2000 (1291), 1965 (411), 1890 (1792)
$a2^{2+}$	2017 ^b , 1967 ^b , 1852 ^b	2006 (387), 1968 (397), 1895 (638)

^aIn parentheses, the computed intensities (in km mol^{-1}). ^bDerived from inspection of the spectra shown in the figures of ref 14.

between Fe_p and Fe_d ($\text{C}-\text{Fe}_p$ distance 2.51 Å, Figure 3). Calculation of overall spin populations and charges of the dinuclear and mononuclear sites shows that the unpaired electron is localized on the former (see Table 1). The metallocene fragment features a zero value for both Mulliken populations instead, as expected for a Fe(II) redox state. IR and EPR measurements on A^+ indicated that the unpaired electron mostly resides on Fe_d ; notably, the computed spin populations of Fe_d and Fe_p centers in a^+ are 0.90 and 0.14, respectively, in full agreement with the experimental picture. DFT vibrational frequencies of carbonyl ligands in a^+ are 1998, 1959, and 1871 cm^{-1} . Comparison with the experimental IR absorption (see Table 2) evidences a fairly good match, with deviations in line with those previously reported for variously substituted CO-bridged and semibridged biomimetic complexes.²⁶ Finally, it was possible to identify a monocationic isomer featuring equatorial orientation of the benzyl group in the pendant (structure shown in the Supporting Information), which however is 2.9 kcal mol^{-1} less favored than the axial model in Figure 3.

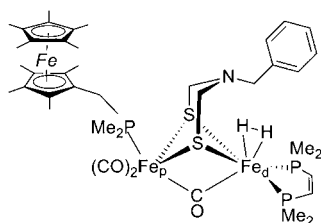
The second oxidation step leads to the dicationic species A^{2+} ; the fact that the IR frequencies of the terminal CO groups shift by only $\sim 4 \text{ cm}^{-1}$ upon $A^+ - e^- \rightarrow A^{2+}$ oxidation indicates that the diiron fragment retains the Fe(II)Fe(I) state. Therefore, the overall oxidation state of the iron atoms in A^{2+} is $\text{Fe(III)Fe(II)Fe(I)}$,¹⁴ as anticipated in the Introduction. Variable-temperature magnetic susceptibility measurements demonstrated that A^{2+} has two unpaired electrons;¹⁴ thus, we considered both an open shell singlet and a triplet for our a^{2+} models. Let us start with a description of the triplet (model $a1^{2+}$, Figure 3). Comparison between $a1^{2+}$ and a^+ shows that the scaled DFT frequencies of the terminal COs in $a1^{2+}$ undergo shifts similar to the experimentally observed ones (Table 2). The semi-bridging CO frequency is overestimated by 38 cm^{-1} , a value in line with the maximum deviation (36.3 cm^{-1}) previously reported for other biomimetic μ -CO species.²⁶ Overall charges and spin populations of $a1^{2+}$ are consistent with the $\text{Fe(III)Fe(II)Fe(I)}$ state (see Table 1); in fact, the charge of the metallocene portion is 1.38 e , and computed spin populations indicate the presence of one unpaired electron at this site. A spin population close to one was computed also for the diiron fragment, with the Fe_d center contribution being the largest (0.89). Variation in Mulliken charges as a result of the $a^+ \rightarrow a1^{2+} + e^-$ oxidation is 1.34 e for the mononuclear portion, while a much smaller variation (0.33 e) was computed for the diiron site. Finally, also in the case of this triplet, it is possible to identify an isomer with equatorial orientation of the benzyl group in the pendant (structure shown in the Supporting Information); such conformation is disfavored with respect to

the axial model in Figure 3 by $2.5 \text{ kcal mol}^{-1}$, analogously to the case of \mathbf{a}^+ (vide supra).

We now focus on the open-shell singlet \mathbf{a}^{2+} , a model featuring spin densities with opposite signs at the level of the dinuclear and mononuclear fragments (Table 1). The computed stability difference between \mathbf{a}^{2+} and \mathbf{a}^{1+} is close to zero ($\Delta E = 0.2 \text{ kcal mol}^{-1}$ in favor of the former). Moreover, the scaled vibrational frequencies of CO groups in \mathbf{a}^{2+} do not differ by more than 6 cm^{-1} from the corresponding ones in \mathbf{a}^{1+} (see Table 2). Mulliken spin population and charge of the dinuclear portion remain essentially unchanged upon $\mathbf{a}^+ \rightarrow \mathbf{a}^{1+} + e^-$ oxidation, as the redox process is localized at the level of the mononuclear moiety in our model (Table 1). Finally, the axial position of the pendant in \mathbf{a}^{2+} is favored over the equatorial counterpart (structure shown in the Supporting Information) by $3.2 \text{ kcal mol}^{-1}$.

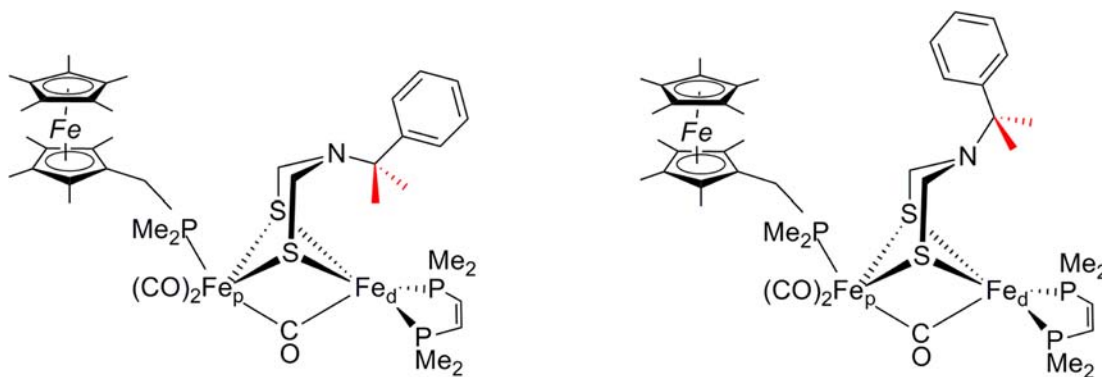
We now turn to the issue of H_2 binding to the dicationic species; in fact, experiments demonstrate that \mathbf{A}^{2+} does interact with dihydrogen by means of its Fe_d center,¹⁴ as mentioned above. This triggers one-electron oxidation of the diiron site at the expense of the metallocene sandwich and concomitant H_2 splitting. As far as our DFT models are concerned, it is noticeable that energy minimization of a $\text{Fe(II)Fe(II)Fe(II)}$ model with dihydrogen nonclassically bound to Fe_d leads to cleavage of the H–H bond along optimization. In other words, if one goes downhill on the potential energy surface starting from the geometry represented in Scheme 3 then one observes

Scheme 3. Initial Structure for Geometry Optimization of $\mathbf{a}^{2+}\text{-2H}$



that one of the two H atoms bound to Fe_d remains attached to the metal center while the other one moves from Fe_d to the amine group of the neighboring pendant. The resulting

Scheme 4. Models Featuring Substitution of the Benzylic Position with Two Methyl Groups (see red bonds in the schematic representations)^a

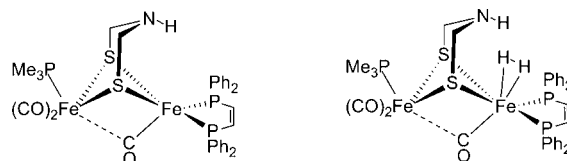


^aThe axial isomer (on the left) and equatorial one (on the right) were computed to be essentially degenerate both in the triplet and in the singlet states ($\Delta E < 0.1 \text{ kcal mol}^{-1}$; see optimized geometries of models $\mathbf{a1_dimethyl}^{2+}$, $\mathbf{a1'_dimethyl}^{2+}$, $\mathbf{a2_dimethyl}^{2+}$, and $\mathbf{a2'_dimethyl}^{2+}$ in the Supporting Information).

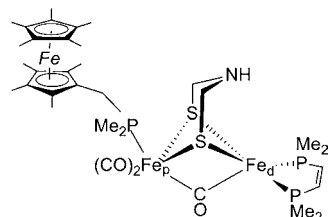
minimum geometry is shown in Figure 3 (model $\mathbf{a}^{2+}\text{-2H}$); the same figure also shows the transition state structure for binding of H_2 to the complex (model $\mathbf{a}_{\text{TS}}^{2+}\text{-H}_2$). Notably, the reaction $\mathbf{a}^{2+} + \text{H}_2 \rightarrow \mathbf{a}^{2+}\text{-2H}$ is associated with a negative energy difference ($-2.7 \text{ kcal mol}^{-1}$) and a low barrier: $+7.8 \text{ kcal mol}^{-1}$. However, from a mechanistic perspective it is important to underline that H_2 splitting with concomitant proton transfer implies axial to equatorial rearrangement of the benzyl group in the pendant. As the transition state for H_2 attachment to Fe_d (see $\mathbf{a}_{\text{TS}}^{2+}\text{-H}_2$ in Figure 3) already shows an equatorial position of the benzyl group in the pendant, we conclude that H_2 binding to the model can occur only after an energetically disfavored axial to equatorial isomerization of \mathbf{A}^{2+} . In view of this, we verified whether targeted structural modification of the dication can lead to stabilization of the equatorial orientation of the bulky group in the pendant. Notably, models featuring substitution of the benzylic position with two methyl groups (see Scheme 4) are such that the axial and equatorial isomers are degenerate (optimized geometries in the Supporting Information).

Comparison between the Reactivity of \mathbf{A}^{2+} and Structurally Related Diiron and Triiron Complexes. In order to gain further insight into the key topic of H_2 splitting on biomimetic compounds, we extended our investigation to selected models structurally related to \mathbf{A}^{2+} . More specifically, in the following we will consider the diiron complex $[\text{Fe}_2((\text{SCH}_2)_2\text{NH})(\text{CO})_3(\text{PMe}_3)(\text{dppv})]^+$ which is known to interact and split H_2 under very harsh conditions (model $\mathbf{a_diiron}^+$ in Scheme 5) as well as model $\mathbf{a_dtma}^{2+}$ (Scheme

Scheme 5. Models $\mathbf{a_diiron}^+$ (on the left) and $\mathbf{a_diiron}^+\text{-H}_2$



6). The latter is a triiron compound that differs from \mathbf{a}^{2+} because the benzyl group in the pendant is substituted with a hydrogen atom, thus giving place to a di(thiomethyl)amine

Scheme 6. Schematic Structure of Model a_dtma^{2+} 

ligand (dtma). Notably, dtma is the azadithiolate component selected by nature for the enzyme active site.

Let us start by discussing results on the dinuclear compound a_diiron^+ . A relevant structural feature of this compound is the presence of the dtma ligand bridging the Fe centers. Moreover, a_diiron^+ lacks any redox-active ligand that can behave as a redox partner for the diiron core. Consequently, the Fe(II)Fe(I) state is retained also after H_2 binding to a_diiron^+ , as intramolecular electron transfer from the diiron site cannot take place in this case. The increase in dihydrogen acidity is therefore not as pronounced as in the case of a^{2+} , a fact that favors the existence of metal–dihydrogen complexes as minima on the potential energy surface (see model $a_diiron^+-H_2$ in Scheme 5 and Supporting Information). As far as H_2 -binding energies are concerned, the reaction $a_diiron^+ + H_2 \rightarrow a_diiron^+-H_2$ ($\Delta E = +6.2$ kcal mol $^{-1}$) is significantly less favored than the corresponding reaction taking place on the trinuclear adduct ($\Delta E = -2.7$ kcal mol $^{-1}$, see above). Finally, notice that $a_diiron^+-H_2$ has axial orientation of the NH group in the pendant. Such isomer is the absolute minimum on the potential energy surface, while the alternative isomer ($a'_diiron^+-H_2$, see Supporting Information) is 0.6 kcal mol $^{-1}$ higher in energy. Notably, previous hybrid quantum mechanical/molecular mechanical results evidenced that H_2 binding to the Fe_d center is compatible with a dtma ligand featuring axial orientation of the NH group also in the $Fe_p(II)Fe_d(I)$ H_{ox} state of [FeFe]-hydrogenases.³⁶

We now turn to the case of the triiron model a_dtma^{2+} .³⁷ Calculations on this compound and derivatives were carried out in order to unveil possible effects of substitution of the benzyl-containing dithiolate ligand in a^{2+} with the naturally occurring dtma. In Figure 4, the optimized geometry of model $a1_dtma^{2+}$ is reported. This is a triplet featuring axial orientation of the NH group in the pendant, which is 2.7 kcal mol $^{-1}$ more stable than the equatorial isomer (model $a1'_dtma^{2+}$, structure shown in the Supporting Information). Similar results were obtained when comparing the open-shell species $a2_dtma^{2+}$ and $a2'_dtma^{2+}$ (structures shown in the Supporting Information): the former is the model with an axial NH group, 2.9 kcal mol $^{-1}$ more stable than the latter which features the equatorial orientation of the amine. Such energy differences are very close to the ones above reported for the axial to equatorial rearrangement in $a1^{2+}$ and $a2^{2+}$. Another analogy with the benzyl-containing model is that interaction between H_2 and the Fe_d center triggers axial to equatorial rearrangement also of the dtma amine group. The H_2 -bound model ($a_dtma^{2+}-H_2$, Figure 4) features a $Fe_p(II)Fe_d(II)$ state of the diiron site and $Fe(II)$ state at the metallocene, as indicated by the overall Mulliken charges of the two portions of the model (1.71 and 0.28 e respectively, values very close to the ones reported for model $a^{2+}-2H$; see Table 1). However, $a_dtma^{2+}-H_2$ features nonclassical coordination of H_2 to Fe_d , at variance with the case of dihydrogen binding to the benzyl-containing

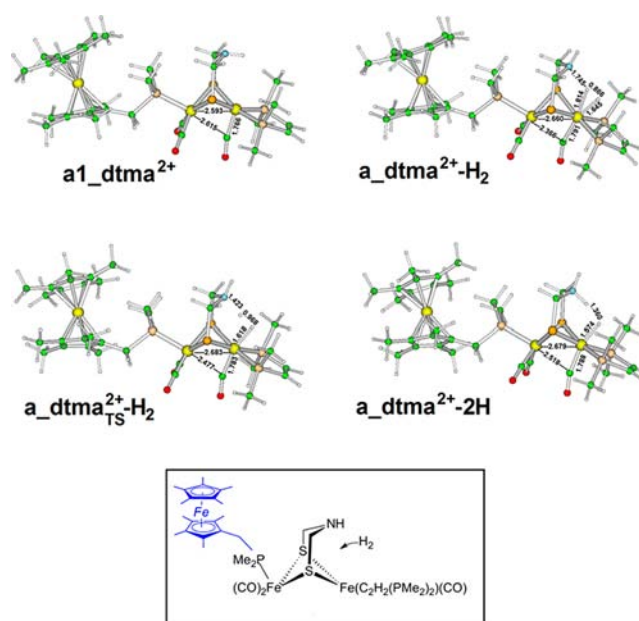
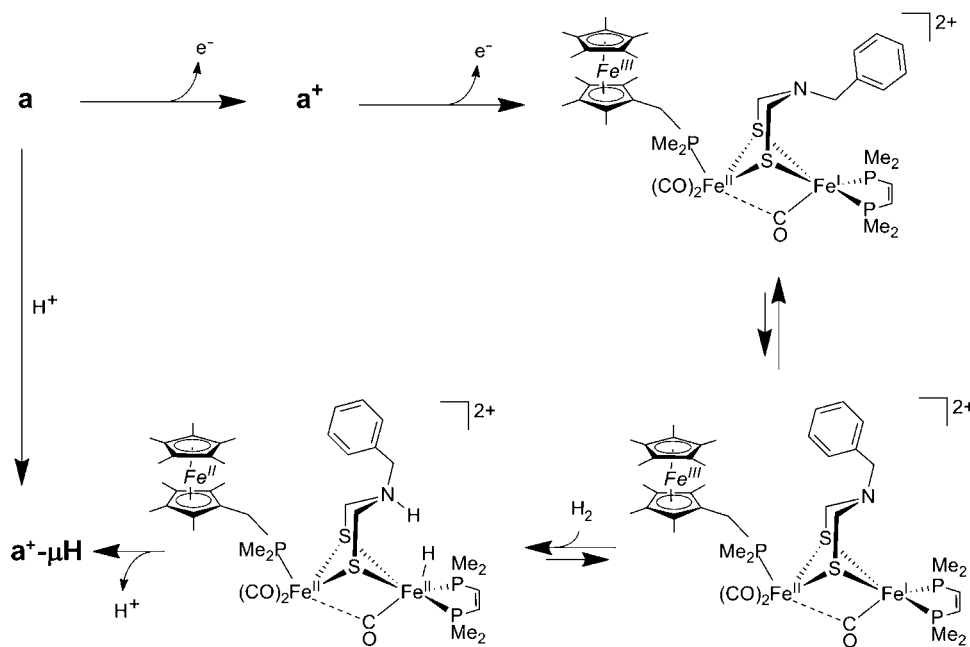


Figure 4. Optimized structures of selected triiron models, with relevant bond distances explicitly marked (all values in Angstroms). Color code is the same as in Figure 3. (Inset) Schematic representation of the models: composition of the diiron and monoiron portions considered for Mulliken population analyses (see Table 1) is highlighted in black and blue, respectively.

model (see above). Such result is in line with the experimental observation that replacement of the benzyl-containing azadithiolate with dtma significantly reduces the reactivity of bioinspired complexes, as hydride formation in the presence of H_2 takes place less efficiently in the latter case.²² The transition state structure for H_2 splitting as well as the corresponding product were also localized (see $a_dtma_{TS}^{2+}-H_2$ and $a_dtma^{2+}-2H$ in Figure 4). The reaction barrier turned out to be as low as 3.2 kcal mol $^{-1}$, and the product is 1.3 kcal mol $^{-1}$ higher in energy than the reactant.

CONCLUSIONS

Using density functional theory for characterization of vibrational properties and intramolecular redox events in hydrogenases models, we deepened insights into the remarkable capacity of the triiron complex **A** to mimic the fundamentals of [FeFe]-hydrogenases chemistry. Theoretical data are consistent with the overall experimental picture, indicating that **A** is able to combine substrate binding, redox, and acid–base functionalities. The A^{2+} isomer competent for H_2 binding turned out to correspond to a local minimum on the potential energy surface (see Scheme 7); notably, H_2 coordination and splitting take place concomitantly on such form of the synthetic catalyst. In fact, the presence of a benzyl moiety at the pendant amine enhances basicity of the latter, thus favoring heterolytic H_2 splitting. On the other hand, the same bulky group impedes H_2 uptake when A^{2+} is in its global minimum. A^{2+} also was unable to form a transient dihydrogen complex, at variance with the case of the enzyme active site.³⁸ In this respect, DFT modeling showed that energy minima featuring side-on coordination of H_2 on Fe_d exist also in the case of a triiron model strictly related to A^{2+} but featuring a di(thiomethyl)amine bridge in place of the benzyl-substituted dithiolate. A dihydrogen complex was localized also on the

Scheme 7. Mechanistic Picture on H₂ Binding and Splitting at the [FeFe]-Hydrogenase Model a, Based on DFT Results

potential energy surface of a previously synthesized diiron compound capable of H₂ splitting.²²

As a whole, our results confirm that targeted application of DFT-based approaches leads to a satisfactory description not only of the vibrational properties of hydrogenases models²⁶ but also of their substrate-dependent redox reactivity.¹⁹

■ ASSOCIATED CONTENT

Supporting Information

Figures with optimized structures of selected models, Mulliken spin populations of metal ions in selected complexes, discussion of structure and reactivity of additional models cited in the paper main text, Cartesian coordinates of the optimized structures illustrated in the figures and schemes. This material is available free of charge via the Internet at <http://pubs.acs.org>.

■ AUTHOR INFORMATION

Corresponding Author

*Phone: +390264482098. E-mail: claudio.greco@unimib.it.

Notes

The authors declare no competing financial interest.

■ ACKNOWLEDGMENTS

Financial support of this work from the Cluster of Excellence "Unifying Concepts in Catalysis" (Berlin) is gratefully acknowledged.

■ REFERENCES

- (1) Cammack, R.; Frey, M.; Robson, R. *Hydrogen as a Fuel: Learning from Nature*; Taylor & Francis: London and New York, 2001.
- (2) Hoffmann, P. *Tomorrow's Energy: Hydrogen, Fuel Cells, and the Prospects for a Cleaner Planet*; The MIT Press: Cambridge, 2002.
- (3) Coontz, R.; Hanson, B. *Science* **2004**, *305*, 957.
- (4) Vignais, P. M.; Billoud, B. *Chem. Rev.* **2007**, *107*, 4206.
- (5) Friedrich, B.; Fritsch, J.; Lenz, O. *Curr. Opin. Biotechnol.* **2011**, *22*, 358.
- (6) Gordon, J. C.; Kubas, G. J. *Organometallics* **2010**, *29*, 4682.
- (7) Wright, J. A.; Turrell, P. J.; Pickett, C. J. *Organometallics* **2010**, *29*, 6146.
- (8) Thauer, R. K.; Kaster, A.-K.; Goenrich, M.; Schick, M.; Hiromoto, T.; Shima, S. *Annu. Rev. Biochem.* **2010**, *79*, 507.
- (9) Shima, S.; Pilak, O.; Vogt, S.; Schick, M.; Stagni, M. S.; Meyer-Klaucke, W.; Warkentin, E.; Thauer, R. K.; Ermler, U. *Science* **2008**, *321*, 572.
- (10) Frey, M. *ChemBioChem* **2002**, *3*, 153.
- (11) Peters, J. W.; Lanzilotta, W. N.; Lemon, B. J.; Seefeldt, L. C. *Science* **1998**, *282*, 1853.
- (12) Nicolet, Y.; Piras, C.; Legrand, P.; Hatchikian, C. E.; Fontecilla-Camps, J. C. *Structure* **1999**, *7*, 13.
- (13) Pandey, A. S.; Harris, T. V.; Giles, L. J.; Peters, J. W.; Szilagy, R. K. *J. Am. Chem. Soc.* **2008**, *130*, 4533.
- (14) Erdem, O. F.; Schwartz, L.; Stein, M.; Silakov, A.; Kaur-Ghumaan, S.; Huang, P.; Ott, S.; Reijerse, E. J.; Lubitz, W. *Angew. Chem., Int. Ed.* **2011**, *50*, 1439.
- (15) Silakov, A.; Wenk, B.; Reijerse, E.; Lubitz, W. *Phys. Chem. Chem. Phys.* **2009**, *11*, 6592.
- (16) Ryde, U.; Greco, C.; De Gioia, L. *J. Am. Chem. Soc.* **2010**, *132*, 4512.
- (17) Lubitz, W.; Reijerse, E.; van Gestel, M. *Chem. Rev.* **2007**, *107*, 4331.
- (18) Greco, C.; Bruschi, M.; Fantucci, P.; Ryde, U.; De Gioia, L. *J. Am. Chem. Soc.* **2011**, *133*, 18742.
- (19) Bruschi, M.; Greco, C.; Kaukonen, M.; Fantucci, P.; Ryde, U.; De Gioia, L. *Angew. Chem., Int. Ed.* **2009**, *48*, 3503.
- (20) Fritsch, J.; Scheerer, P.; Frielingsdorf, S.; Kroschinsky, S.; Friedrich, B.; Lenz, O.; Spahn, C. M. T. *Nature* **2011**, *479*, 249.
- (21) Si, Y. T.; Charreter, K.; Capon, J. F.; Gloaguen, F.; Petillon, F. Y.; Schollhammer, P.; Talarmin, J. J. *Inorg. Biochem.* **2010**, *104*, 1038.
- (22) Camara, J. M.; Rauchfuss, T. B. *Nat. Chem.* **2012**, *4*, 26.
- (23) Liu, Y. C.; Lee, C. H.; Lee, G. H.; Chiang, M. H. *Eur. J. Inorg. Chem.* **2011**, 1155.
- (24) de Hatten, X.; Bothe, E.; Merz, K.; Huc, I.; Metzler-Nolte, N. *Eur. J. Inorg. Chem.* **2008**, 4530.
- (25) Tard, C.; Liu, X. M.; Ibrahim, S. K.; Bruschi, M.; De Gioia, L.; Davies, S. C.; Yang, X.; Wang, L. S.; Sawers, G.; Pickett, C. J. *Nature* **2005**, *433*, 610.
- (26) Schwab, D. E.; Tard, C.; Brecht, E.; Peters, J. W.; Pickett, C. J.; Szilagy, R. K. *Chem. Commun.* **2006**, 3696.
- (27) Topf, C.; Monkowius, U.; Knor, G. *Inorg. Chem. Commun.* **2012**, *21*, 147.
- (28) Bott, S. G.; Yang, K. Y.; Richmond, M. G. *J. Organomet. Chem.* **2006**, *691*, 3771.
- (29) Yang, K. Y.; Smith, J. M.; Bott, S. G.; Richmond, M. G. *Organometallics* **1993**, *12*, 4779.
- (30) Yang, K. Y.; Bott, S. G.; Richmond, M. G. *Organometallics* **1995**, *14*, 2387.
- (31) Yang, K. Y.; Bott, S. G.; Richmond, M. G. *J. Organomet. Chem.* **1996**, *516*, 65.
- (32) Kandala, S.; Hammons, C.; Watson, W. H.; Wang, X. P.; Richmond, M. G. *Dalton*

Trans. **2010**, *39*, 1620. Mao, F.; Tyler, D. R.; Keszler, D. *J. Am. Chem. Soc.* **1989**, *111*, 130. Tyler, D. R. *Acc. Chem. Res.* **1991**, *24*, 325.

(18) Tard, C.; Pickett, C. *J. Chem. Rev.* **2009**, *109*, 2245. Thomas, C. M.; Liu, T. B.; Hall, M. B.; Darensbourg, M. Y. *Inorg. Chem.* **2008**, *47*, 7009. Wang, N.; Wang, M.; Zhang, T. T.; Li, P.; Liu, J. H.; Sun, L. C. *Chem. Commun.* **2008**, 5800. Ezzaher, S.; Capon, J. F.; Dumontet, N.; Gloaguen, F.; Petillon, F. Y.; Schollhammer, P.; Talarmin, J. *J. Electroanal. Chem.* **2009**, *626*, 161. van der Vlugt, J. I.; Rauchfuss, T. B.; Whaley, C. M.; Wilson, S. R. *J. Am. Chem. Soc.* **2005**, *127*, 16012. Chen, Z. J.; Lemon, B. J.; Huang, S.; Swartz, D. J.; Peters, J. W.; Bagley, K. A. *Biochemistry* **2002**, *41*, 2036. Olsen, M. T.; Rauchfuss, T. B.; Wilson, S. R. *J. Am. Chem. Soc.* **2010**, *132*, 17733. Cheah, M. H.; Borg, S. J.; Best, S. P. *Inorg. Chem.* **2007**, *46*, 1741.

(19) Greco, C.; De Gioia, L. *Inorg. Chem.* **2011**, *50*, 6987.

(20) Liu, Y. C.; Yen, T. H.; Tseng, Y. J.; Hu, C. H.; Lee, G. H.; Chiang, M. H. *Inorg. Chem.* **2012**, *51*, 5997.

(21) Camara, J. M.; Rauchfuss, T. B. *J. Am. Chem. Soc.* **2011**, *133*, 8098.

(22) Olsen, M. T.; Barton, B. E.; Rauchfuss, T. B. *Inorg. Chem.* **2009**, *48*, 7507.

(23) Darensbourg, M. Y.; Bethel, R. D. *Nat. Chem.* **2012**, *4*, 11.

(24) Bertini, L.; Greco, C.; Bruschi, M.; Fantucci, P.; De Gioia, L. *Organometallics* **2010**, *29*, 2013. Bertini, L.; Greco, C.; De Gioia, L.; Fantucci, P. *J. Phys. Chem. A* **2009**, *113*, 5657.

(25) Greco, C.; Bruschi, M.; Fantucci, P.; De Gioia, L. *Eur. J. Inorg. Chem.* **2007**, 1835.

(26) Yu, L.; Greco, C.; Bruschi, M.; Ryde, U.; De Gioia, L.; Reiher, M. *Inorg. Chem.* **2011**, *50*, 3888.

(27) Ahlrichs, R.; Bar, M.; Haser, M.; Horn, H.; Kolmel, C. *Chem. Phys. Lett.* **1989**, *162*, 165.

(28) Becke, A. D. *Phys. Rev. A* **1988**, *38*, 3098. Perdew, J. P. *Phys. Rev. B* **1986**, *33*, 8822. Eichkorn, K.; Treutler, O.; Ohm, H.; Haser, M.; Ahlrichs, R. *Chem. Phys. Lett.* **1995**, *240*, 283. Eichkorn, K.; Weigend, F.; Treutler, O.; Ahlrichs, R. *Theor. Chem. Acc.* **1997**, *97*, 119. Schafer, A.; Huber, C.; Ahlrichs, R. *J. Chem. Phys.* **1994**, *100*, 5829.

(29) Greco, C.; Bruschi, M.; Fantucci, P.; De Gioia, L. *J. Organomet. Chem.* **2009**, *694*, 2846.

(30) Young, D. *Computational Chemistry*; John Wiley & Sons: New York, 2001.

(31) Greco, C.; Zampella, G.; Bertini, L.; Bruschi, M.; Fantucci, P.; De Gioia, L. *Inorg. Chem.* **2007**, *46*, 108.

(32) Noodleman, L.; Norman, J. G. *J. Chem. Phys.* **1979**, *70*, 4903. Noodleman, L. *J. Chem. Phys.* **1981**, *74*, 5737. Greco, C.; Fantucci, P.; Ryde, U.; de Gioia, L. *Int. J. Quantum Chem.* **2011**, *111*, 3949.

(33) Becke, A. D. *J. Chem. Phys.* **1993**, *98*, 5648. Lee, C. T.; Yang, W. T.; Parr, R. G. *Phys. Rev. B* **1988**, *37*, 785.

(34) Matito, E.; Sola, M. *Coord. Chem. Rev.* **2009**, *253*, 647. Duclausaud, H.; Borshch, S. A. *J. Am. Chem. Soc.* **2001**, *123*, 2825. Poblet, J. M.; Lopez, X.; Bo, C. *Chem. Soc. Rev.* **2003**, *32*, 297.

(35) Nicolet, Y.; de Lacey, A. L.; Verne de, X.; Fernandez, V. M.; Hatchikian, E. C.; Fontecilla-Camps, J. C. *J. Am. Chem. Soc.* **2001**, *123*, 1596.

(36) Greco, C.; Bruschi, M.; De Gioia, L.; Ryde, U. *Inorg. Chem.* **2007**, *46*, 5911.

(37) In principle, $\mathbf{a_dtma}^{2+}$ could be obtained by two subsequent one-electron oxidations of the corresponding neutral model. Therefore, we optimized also the neutral and monocationic models $\mathbf{a_dtma}$ and $\mathbf{a_dtma}^+$ (structures not shown), and in Table 1 we report Mulliken spin populations and charges for the mononuclear and dinuclear portions that compose such models. Results indicate that $\mathbf{a_dtma}$ and $\mathbf{a_dtma}^+$ attain the $Fe(II)Fe(I)Fe(I)$ and $Fe(II)Fe(II)Fe(I)$ redox states, respectively, analogously to the case of \mathbf{a} and \mathbf{a}^+ .

(38) Bruschi, M.; Zampella, G.; Fantucci, P.; De Gioia, L. *Coord. Chem. Rev.* **2005**, *249*, 1620.